Nanoscale

PAPER

View Article Online
View Journal | View Issue

Cite this: *Nanoscale*, 2017, **9**, 16313

Engineering a nanotubular mesoporous cobalt phosphide electrocatalyst by the Kirkendall effect towards highly efficient hydrogen evolution reactions†

Yue-E Miao,*[a] Fei Li,[a] Yu Zhou,[a] Feili Lai,[b] Hengyi Lu[b] and Tianxi Liu *[a,b]

Tailoring the size and controlling the morphology of particular nano-architectures are considered as two promising strategies to improve the catalytic performance of metal nanocrystals towards hydrogen evolution reactions (HERs). Herein, mesoporous cobalt phosphide nanotubes (CoP-NTs) with a three-dimensional network structure have been obtained through a facile and efficient electrospinning technique combined with thermal stabilization and phosphorization treatments. The thermal stabilization process has been demonstrated to play a key role in the morphological tailoring of Co_3O_4 nanotubes (Co_3O_4-NTs). As a result, the CoP-NTs show one-dimensional hollow tubular architecture instead of forming a worm-like tubular CoP structure (W-CoP-NTs) or severely aggregated CoP powder (CoP-NPs) which originate from the Co_3O_4 nanotubes without thermal stabilization treatment and Co_3O_4 nanoparticles, respectively. Satisfyingly, under an optimized phosphorization degree, the CoP-NT electrode exhibits a low onset overpotential of 53 mV with a low Tafel slope of 50 mV dec^{-1} during the HER process. Furthermore, the CoP-NT electrode is capable of driving a large cathodic current density of 10 mA cm^{-2} at an overpotential of 152 mV, which is much lower than those of its contrast samples, *i.e.* CoP-NPs (211 mV) and W-CoP-NTs (230 mV). Therefore, this work provides a feasible and general strategy for constructing three-dimensionally organized mesoporous non-noble metal phosphide nanotubes as promising alternative high-performance electrocatalysts for the commercial platinum ones.

Received 7th August 2017,
Accepted 23rd September 2017

DOI: 10.1039/c7nr05825j

rsc.li/nanoscale

Introduction

Hydrogen, as a renewable and clean energy carrier, has been considered as a promising alternative to meet the ever-increasing global energy demands.[1,2] To produce hydrogen with high purity, water electrolysis has become one of the most efficient approaches. However, it heavily relies on the efficiency of the cathode electrocatalyst to minimize the overpotential during the hydrogen evolution reaction (HER) process.[3,4] As one of the most widely used HER catalysts, platinum (Pt) requires very low overpotential to generate large cathodic current density in highly acidic solutions.[5–7] Nevertheless, its large-scale application is severely limited due to the low abundance and high price of noble metals. Therefore, considerable research efforts have been made to develop earth-abundant non-noble metal HER catalysts.[8] Generally, an ideal HER electrocatalyst should feature several prominent characteristics, including a porous structure to enable fast mass transport, good electrical conductivity to facilitate rapid electron transfer, high aspect ratio and nanoscale dimensions to maximize the number of exposed active sites per geometric area.[9–11] As expected, transition metal phosphides (TMPs) consisting of metal and phosphorus alloys show good electrical conductivity as alternative nonprecious acid-stable HER catalysts.[12–14] The well-described HER volcano suggests that TMPs are among the best possible catalysts in terms of their high affinities for H_2. In particular, cobalt phosphides (CoP) have emerged as a new class of the most active and efficient metal phosphide catalysts with an optimum hydrogen adsorption free energy close to the top of the HER volcano.[15] Nevertheless, the intrinsic high surface energy and severe aggregation of nanoparticles easily lead to decreased active catalytic sites, which relatively confine their total electrode activity and average turnover frequency per surface site.

[a]*State Key Laboratory for Modification of Chemical Fibers and Polymer Materials, College of Materials Science and Engineering, Donghua University, Shanghai 201620, China. E-mail: yuee_miao@dhu.edu.cn, txliu@dhu.edu.cn*
[b]*State Key Laboratory of Molecular Engineering of Polymers, Department of Macromolecular Science, Fudan University, Shanghai 200433, China. E-mail: txliu@fudan.edu.cn*

†Electronic supplementary information (ESI) available: Photographs of Co_3O_4-NTs, W-Co_3O_4-NTs and Co_3O_4-NPs. TEM images of Co_3O_4-NTs. FESEM image and the corresponding EDS elemental mappings of CoP-NTs. BET analysis of CoP-NPs and CoP-NTs. XRD patterns of Co_3O_4-NTs and CoP-NTs with different phosphorization degrees. See DOI: 10.1039/c7nr05825j

As the catalytic efficiency of an electrocatalyst largely depends on its surface properties, structural engineering is of great importance in the construction of dominant nanostructures for CoP-based catalysts to effectively increase their exposed active edges.[16,17] Notably, CoP-based electrocatalysts with different nano-architectures of nanowires,[18] nanorods,[19,20] nanocubes,[21] and nanoparticles[22] have been developed through feasible geometric constructions. In particular, hollow nanostructures have aroused increasing attention among various nano-architectures for electrochemical energy conversion and storage applications, due to their outstanding features of well-defined interior voids, high specific surface area, and significantly shortened mass/charge transport lengths.[23,24] For example, multifaceted CoP hollow quasi-spheres with an average diameter of 13 ± 2 nm have been reported through the stepwise transformation of Co nanoparticles into Co_2P and CoP nanoparticles by reaction with tri-*n*-octylphosphine.[25] As a result of the Kirkendall effect, the hollow nanostructured CoP electrocatalyst exhibits high efficiency and acid-stability by exposing and stabilizing more active sites toward sufficient mass transport. Ni–Co Prussian blue analogue nanocubes also have been used as sacrificial templates to synthesize unique nickel cobalt phosphide quasi-hollow nanocubes.[21] As expected, due to their structural and compositional merits, the nickel cobalt phosphide quasi-hollow nanocubes present excellent electrochemical performance with a low overpotential of 150 mV to afford a high current density of 10 mA cm^{-2} and a low Tafel slope of 60.1 mV dec^{-1} for hydrogen evolution reactions in alkaline solution. Although considerable progress has been made above, the involvement of several kinds of organic solvents and multiple tedious steps may introduce inferior long-range order or structural control in these CoP micro/nanostructures, thus leading to limited charge transport and possible deactivation. For this reason, it is extremely expected to develop high-performance CoP-based HER electrocatalysts by feasibly constructing hollow nanostructures with effectively increased exposed active edges and conductive pathways toward efficient hydrogen evolution reactions.

Herein, we demonstrate a universal and effective electrospinning technique to fabricate well-defined one-dimensional (1D) CoP nanotubes (CoP-NTs) with a high aspect ratio, porous structure and abundant active sites for HER applications as illustrated in Fig. 1a. Combined with the facile pre-oxidization, calcination and low-temperature phosphorization processes, this highly tunable synthesis offers several advantages: (i) the electrospinning technique easily produces a three-dimensional (3D) network consisting of 1D interconnected CoP channels with a high aspect ratio and long-range order, which will largely improve the exposed active sites of CoP-NTs per geometric area; (ii) benefitting from the Kirkendall effect combined with a controlled thermal stabilization treatment, mesoporous CoP-NTs composed of small nanoparticles (approximately 5–10 nm in diameter) on the nanotube walls are successfully obtained, to achieve a greatly increased specific surface area and rich basal edges in radial directions compared with the severely aggregated CoP nanoparticles; (iii) attributed to the simultaneously facilitated mass transport and electron transfer, the CoP-NT electrode shows significantly enhanced HER performance with a low onset overpotential of 53 mV and a low overpotential of 152 mV to drive a large current density of 10 mA cm^{-2}, being a promising non-noble metal HER electrocatalyst.

Experimental

Materials

Polyvinylpyrrolidone (PVP, M_w = 1 300 000 g mol^{-1}) was purchased from Sigma-Aldrich. *N*,*N*-Dimethylformamide (DMF), 98% H_2SO_4, hydrochloric acid, $Co(Ac)_2{\cdot}4H_2O$ and NaH_2PO_2

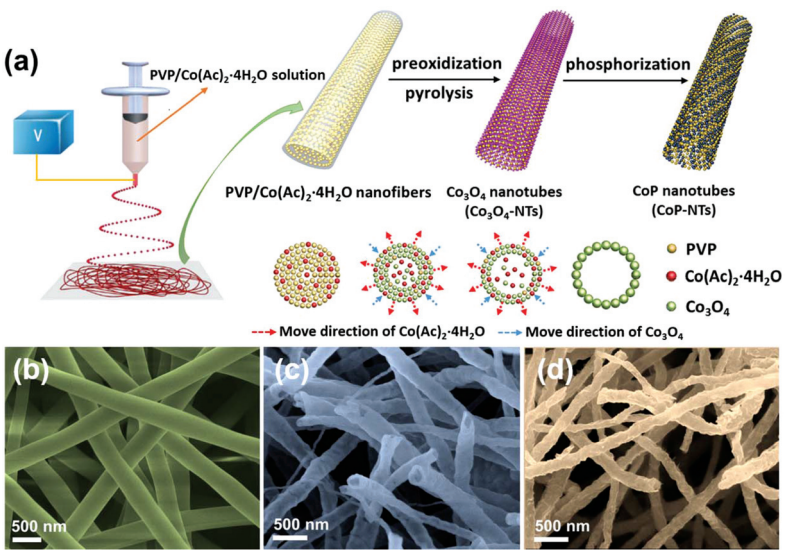

Fig. 1 (a) Schematic illustration for the preparation of CoP-NTs; FESEM images of (b) PVP/$Co(Ac)_2{\cdot}4H_2O$ nanofibers, (c) Co_3O_4-NTs and (d) CoP-NTs.

were supplied by Sinopharm Chemical Reagent Co., Ltd. The Pt/C catalyst (20 wt% platinum on carbon black) was purchased from Alfa Aesar. Deionized water (DI water) was used throughout the experiments. All other reagents were of analytical grade and used as received without further treatments.

Preparation of electrospun cobalt oxide nanotubes

During a typical electrospinning process,[26,27] 2.0 g of $Co(Ac)_2{\cdot}4H_2O$ and 1.5 g of PVP were dissolved in 9.0 g of DMF in turn, followed by a continuous magnetic stirring at ambient temperature to yield a homogeneous solution. Then, the precursor solution was loaded into a plastic syringe at a flow rate of 0.1 mL min^{-1}. A high-voltage power of 20 kV was applied to the needle tip, while the distance between the needle tip and collector is set as 20 cm. Subsequently, the as-collected PVP/$Co(Ac)_2{\cdot}4H_2O$ fiber membrane was thermally treated under an air atmosphere at 200 °C with a ramping rate 2 °C min^{-1} and stabilized for 3 h. Then, the samples were annealed at 550 °C for 2 h under an air atmosphere to remove PVP and obtain Co_3O_4 nanotubes, which are labeled as Co_3O_4-NTs.

For comparison, Co_3O_4 nanotubes, prepared under the same annealing conditions from the PVP/$Co(Ac)_2{\cdot}4H_2O$ fiber membrane but without the thermal stabilization treatment at 200 °C, were obtained and labeled as W-Co_3O_4-NTs. Co_3O_4 nanoparticles, labelled as Co_3O_4-NPs, were also obtained *via* the high-speed ball milling and pulverization of Co_3O_4-NTs.

Preparation of cobalt phosphide nanotubes

To figure out the optimal phosphorization degree of Co_3O_4-NTs, a certain amount of Co_3O_4-NTs was mixed with NaH_2PO_2 homogeneously at fixed mass ratios of 1 : 2, 1 : 5, 1 : 8, and 1 : 11 for Co_3O_4-NTs and NaH_2PO_2, respectively. Then, the mixtures were annealed at 300 °C for 2 h at a heating rate of 2 °C min^{-1} under an Ar atmosphere. The as-obtained products were washed with deionized water and hydrochloric acid several times and dried at 80 °C for 8 h, thus resulting in the cobalt phosphide nanotubes of CoP-NTs-2, CoP-NTs-5, CoP-NTs-8 and CoP-NTs-11, respectively.

For comparison, certain amounts of W-Co_3O_4-NTs and Co_3O_4-NPs were mixed with NaH_2PO_2 at a fixed mass ratio of 1 : 8, respectively, and then underwent the same phosphorization reaction to obtain W-CoP-NTs and CoP-NPs.

Characterization

Morphology of the samples was observed using a field emission scanning electron microscope (FESEM, Zeiss) at an acceleration voltage of 5 kV, which is attached with an energy dispersive X-ray spectrometer. Transmission electron microscopy (TEM) was performed under an acceleration voltage of 200 kV with a Tecnai G2 20 TWIN TEM. X-ray diffraction (XRD) experiments were conducted from 2θ = 5° to 70° on an X'Pert Pro X-ray diffractometer with Cu K_α radiation (λ = 0.1542 nm) under a voltage of 40 kV and a current of 40 mA. Brunauer–Emmett–Teller (BET) nitrogen adsorption–desorption isotherms were measured using a Quantachrome Autosorb-iQ/MP®XR system. X-ray photoelectron spectroscopy (XPS) analyses were carried out on a Thermo Scientific ESCALAB 250Xi system using an Al K_α source of 1486.6 eV. All XPS spectra were corrected using the C 1s line at 284.6 eV, while curve fitting and background subtraction were accomplished using the RBD AugerScan 3.21 software.

Electrochemical measurements

All electrochemical measurements were performed on a CHI 660D electrochemical workstation (Shanghai Chenhua Instrument Co., China). A standard three-electrode setup was adopted at room temperature, where the glassy carbon electrode (GCE), graphite rod and saturated calomel electrode (SCE) were respectively used as the working, counter and reference electrodes. Prior to all electrochemical measurements, the GCE was sequentially polished with 1.0, 0.3 and 0.05 μm alumina slurries, and then cleaned with HNO_3, ethanol and deionized water, respectively. Afterwards, the electrode was left to dry under a N_2 stream. Then, 2 mg of the samples was dispersed in 200 μL of water along with 20 μL Nafion (5 wt% in ethanol) and sonicated for at least 15 min to form a homogeneous emulsion. Finally, 2.5 μL of the above slurry was dropped onto the GCE with a diameter of 3 mm to form the sample modified GCE with a loading amount of 0.35 mg cm^{-2}. For comparison, the commercially available Pt/C modified electrode was also prepared in the same way.

All the measurements were performed in nitrogen purged 0.5 M H_2SO_4 solution. The linear sweep voltammetry measurements were performed at a sweep rate of 2 mV s^{-1}, while the final potential was calibrated to the reversible hydrogen electrode (RHE) by adding a value of (0.241 + 0.059pH) V. The polarization curves were then expressed as the overpotential (η) *vs.* log current density ($\log(j)$) to obtain the Tafel plots. Subsequently, the Tafel slope (b) was obtained by fitting the linear portion of the Tafel plots to the Tafel equation ($\eta = b \log(j) + a$). The onset overpotential was determined from the starting point of the linear regime in the Tafel plot. Electrochemical impedance spectroscopy (EIS) measurements were conducted by applying an AC voltage in the frequency range between 100 kHz and 10 mHz with an amplitude of 5 mV. Cyclic voltammetry (CV) sweeps were collected between −0.4 V and +0.6 V at a scan rate of 2 mV s^{-1}. The durability test was carried out by collecting the time-dependent current density curve under a static overpotential of 170 mV.

Results and discussion

Electrospinning is a simple and efficient technique for fabricating self-standing nanofiber membranes with a unique three-dimensional network, high porosity and good structural stability.[28–30] In this work, 1D inorganic salt-containing PVP nanofibers (PVP/$Co(Ac)_2{\cdot}4H_2O$) with a smooth surface and diameter around 400 nm (Fig. 1b) are facilely obtained *via* the electrospinning of a viscous homogeneous precursor solution. By thermal stabilization and pyrolysis of the PVP/$Co(Ac)_2{\cdot}4H_2O$ nanofiber membrane under an air atmosphere, PVP first pyro-

lyzes and shrinks as the temperature slowly increases. At the same time, $Co(Ac)_2{\cdot}4H_2O$ moves to the fiber surface and decomposes into Co_3O_4 at a relatively high speed. Initiated by this Kirkendall effect as illustrated in Fig. 1a, Co_3O_4-NTs are eventually obtained. To be emphasized is that thermal stabilization of the PVP/$Co(Ac)_2{\cdot}4H_2O$ nanofiber membrane before pyrolysis is extremely necessary to achieve the light-weight Co_3O_4-NT membrane with a well-maintained macroscopic structure as shown in Fig. S1a.† Otherwise, only curled and collapsed Co_3O_4 bulks (Fig. S1b†) can be obtained from the PVP/$Co(Ac)_2{\cdot}4H_2O$ nanofiber membrane without thermal stabilization treatment, which is more likely to collapse into powdery Co_3O_4 nanoparticle aggregates (Co_3O_4-NPs) as displayed in Fig. S1c.† Fig. 1c reveals that the hollow tubular Co_3O_4-NTs have an average diameter around 320 nm and a rough porous surface without beads or breakages. The TEM image in Fig. S2a† indicates that Co_3O_4-NTs are densely packed with Co_3O_4 nanoparticles with an average size of about 20–30 nm. Moreover, a lattice distance of 0.467 nm can be observed from the high-resolution TEM (HRTEM) image in Fig. S2b,† which is in good accord with the (111) plane of Co_3O_4 nanocrystals. After phosphorization, CoP-NTs with the diameter around 350 nm show a well reserved hollow tubular structure (Fig. 1d), without significant changes compared with that of Co_3O_4-NTs at low magnification. The corresponding energy dispersive X-ray spectroscopy (EDS) analysis clearly reveals the elemental mappings of Co and P elements in Fig. S3,† exhibiting a homogeneous distribution of the Co and P elements over the entire nanotube. However, after the low-temperature phosphorization reaction from the original W-Co_3O_4-NTs with many randomly distributed holes on the nanotube walls (Fig. 2a), only worm-like CoP nanotubes (W-CoP-NTs) with serious deformation and damage of the nano-tubular structure are obtained (Fig. 2b), which further indicates that the thermal stabilization treatment plays a key role in the stabilization of the hollow tubular structure of Co_3O_4-NTs during the high-temperature pyrolysis process. Moreover, the contrast sample of CoP-NPs synthesized from Co_3O_4-NPs also severely aggregates into large particulate aggregations (Fig. 2c and d), implying the significance of the electrospun Co_3O_4-NT template for effectively dispersing the gradually formed CoP nanocrystals.

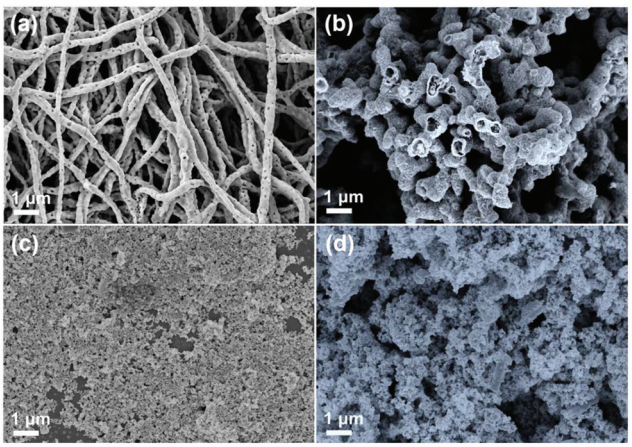

Fig. 2 FESEM images of (a) W-Co_3O_4-NTs, (b) W-CoP-NTs, (c) Co_3O_4-NPs and (d) CoP-NPs.

The morphology of the as-synthesized CoP-NTs is further characterized by transmission electron microscopy. As shown in Fig. 3a, a more amorphous structure is observed for CoP-NTs compared to Co_3O_4-NTs, indicating that the Co_3O_4 nanocrystals are successfully converted into much smaller CoP nanocrystals with the diameter around 5–10 nm in the closely interconnected networks of CoP-NTs. The HRTEM image further shows a lattice distance of 0.238 nm for CoP-NTs (Fig. 3b), which corresponds to the (111) plane of CoP nanocrystals.[22] It has been reported that during the heat treatment, sodium hypophosphite hydrate (NaH_2PO_2) is thermally decom-

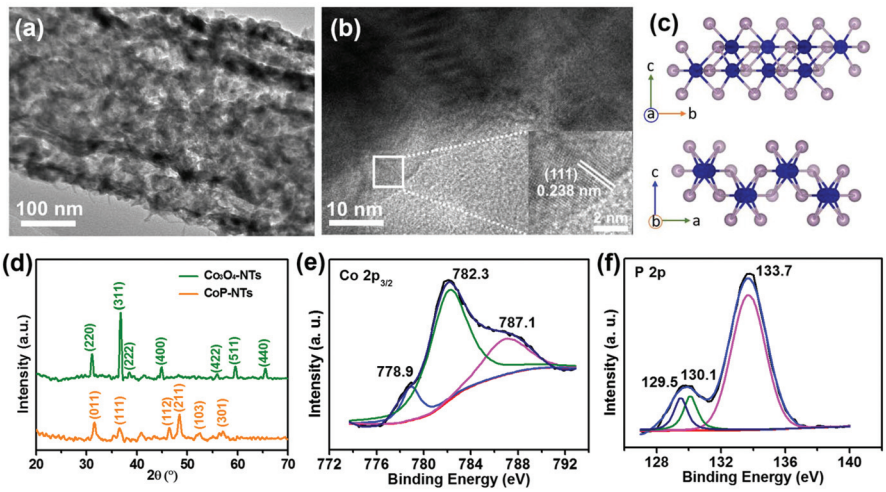

Fig. 3 (a) TEM and (b) HRTEM images of CoP-NTs. (c) Two-direction views of the crystal structure of CoP-NTs, in which blue and pink spheres represent Co and P atoms, respectively. (d) XRD patterns of Co_3O_4-NTs and CoP-NTs. XPS spectra of CoP-NTs: (e) Co 2p; (f) P 2p.

posed to release phosphine, which can reduce Co_3O_4 into Co, and the Co atom will catalyze the decomposition of phosphine to produce P atoms *vice versa*.[31,32] Consequently, the P atom further reacts with Co to form the CoP alloy, thus leading to the conversion of oxides into phosphides with orderly packed crystal structures and mesoporous architectures. From the perspective of the atom structure as illustrated in Fig. 2c, the CoP adopts a MnP-type structure,[22] in which the Co atom is neighbored with six near P atoms to form a distorted face-sharing CoP_6 octahedra configuration, while the P atom is surrounded by six Co atoms with a disordered edge-sharing PCo_6 trigonal prism structure. As a result, the CoP-NTs can provide more sufficiently exposed active edges for H^+ adsorption, H_2 generation and bubble release.

XRD patterns are obtained to further demonstrate the crystal structure of CoP-NTs. As shown in Fig. 3d, sharp diffraction peaks at 2θ = 31.3°, 36.9°, 44.9°, 59.4° and 65.2° are observed in the XRD pattern of Co_3O_4-NTs, corresponding to the (220), (311), (400), (511) and (440) planes of Co_3O_4 nanocrystals (JCPDS 42-1467), respectively.[33] After phosphorization, diffraction peaks occur at 2θ = 31.7°, 36.5°, 48.5°, 52.0° and 57.2° for CoP-NTs, which are respectively indexed to the (011), (111), (211), (103) and (301) crystal planes of CoP (JCPDS 29-0497), indicating the successful conversion of Co_3O_4-NTs into CoP-NTs.[34] XPS characterization is carried out to analyze the surface elemental composition and chemical state of CoP-NTs. Fig. 3e shows that the Co $2p_{3/2}$ region can be deconvolved into two main peaks at 778.9 eV and 782.3 eV with one satellite peak at 787.1 eV, while the high-resolution P 2p region exhibits two peaks at 129.5 eV and 130.1 eV, along with a broad peak at 133.7 eV (Fig. 3f). The peaks at 778.9 eV and 129.5 eV are assigned to the binding energies of Co $2p_{3/2}$ and P $2p_{3/2}$ in CoP.[17] Meanwhile, the peaks at 782.3 eV and 133.7 eV reflect the binding energies of unresolved Co $2p_{3/2}$ and P 2p arising from the oxidized Co and P species, respectively.[35] These results suggest that the Co in CoP partially carries a positive charge, while P partially carries a negative charge, thus leading to the electron transfer from Co to P. As a result, Co and P atoms can function as the hydride-acceptor and proton-acceptor centers respectively for facilitated HER processes.

The electrocatalytic activity of CoP-based electrodes toward the HER was investigated in 0.5 M H_2SO_4 solution using a typical three-electrode setup. The linear sweep voltammetry (LSV) measurements in Fig. 4a clearly show that a low onset overpotential (η) of 53 mV *vs.* RHE is achieved for the CoP-NT electrode at a mass loading of 0.35 mg cm^{-2}, which is most close to the near zero onset overpotential of Pt/C. Moreover, the CoP-NT electrode exhibits better electrocatalytic performance than bulk CoP-NP aggregates and W-CoP-NTs, which show inferior onset overpotentials of 73 mV and 59 mV, respectively. Another important evaluation criterion for HER performance is the cathodic current density. As displayed in Fig. 4a, to drive a high cathodic current density of 10 mA cm^{-2}, an overpotential of 152 mV is necessary for the CoP-NT electrode, which is much lower than those of CoP-NPs (211 mV) and W-CoP-NTs (230 mV). As compared to many

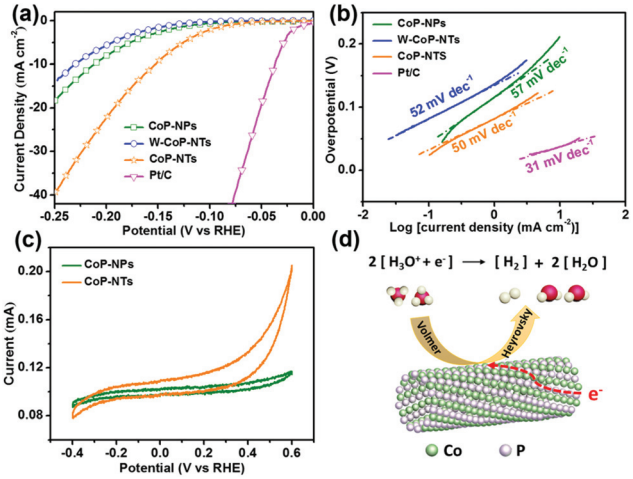

Fig. 4 (a) LSV polarization curves at a scan rate of 2 mV s^{-1}. (b) The corresponding Tafel plots of CoP-NPs, W-CoP-NTs, CoP-NTs and Pt/C, respectively. (c) CV curves of CoP-NPs and CoP-NTs recorded between −0.4 V and +0.6 V at a scan rate of 2 mV s^{-1}. (d) Illustration of the electron transfer and hydrogen evolution process on the surface of CoP-NTs.

other non-noble metal-based electrocatalysts, the CoP-NT electrode possesses a lower overpotential than many previously reported results for the HER in acid media (Table S1†), such as CoP@C core–shell nanocables (η10 mA cm^{-2} = 170 mV),[36] WP_2 submicroparticles (η10 mA cm^{-2} = 161 mV),[37] nanoporous FeP nanosheets (η10 mA cm^{-2} = 240 mV),[38] Co_9S_8@MoS_2/carbon nanofibers (η10 mA cm^{-2} = 190 mV),[39] and Co–Te–Se nanocompound (η10 mA cm^{-2} = 217 mV).[40] To get further insight into the CoP-based electrodes, the corresponding Tafel plots (Fig. 4b) are fitted into the Tafel equation ($\eta = b\log j + a$), where j is the current density, b is the Tafel slope, and a is the intercept relative to the exchange current density. A Tafel slope of 50 mV dec^{-1} is obtained for CoP-NTs, indicating a Volmer–Heyrovsky mechanism which experiences a rapid discharge Volmer reaction followed by a rate-limiting electrochemical desorption Heyrovsky reaction. The remarkably improved catalytic performance of CoP-NTs over CoP-NPs and W-CoP-NTs can be attributed to the unique 1D hollow tubular structure instead of the severe aggregations, thus providing a long range order and a large specific surface area for efficient electrochemical interactions between the electrolyte and electrocatalyst. Additionally, the overall 3D hierarchical architecture of the CoP-NT electrode can provide a significantly shortened ion diffusion length and facilitated electron transfer pathways for fast catalytic hydrogen evolution reactions at the surface of electrochemically active CoP-NTs. Furthermore, EIS tests were carried out to prove the enhanced conductivity of CoP-NTs during the HER process as shown in Fig. S4.† An apparent decrease of the charge-transfer resistance can be observed for the CoP-NT electrode compared to those of CoP-NPs and W-CoP-NTs. Therefore, the CoP-NT electrode exhibits better electrocatalytic performance than bulk CoP-NP aggregates and W-CoP-NTs.

To figure out the microporous structures inside the CoP-NT catalyst, the BET specific surface area and pore size distributions of the samples were determined from adsorption/desorption isotherms. As shown in Fig. S5,† CoP-NTs exhibit a high BET surface area of about 80.4 $m^2 g^{-1}$, while the values are only 14.6 $m^2 g^{-1}$ and 21.0 $m^2 g^{-1}$ for CoP-NPs and W-CoP-NTs, respectively. The Barrett–Joyner–Halenda pore-size-distribution curve of CoP-NTs shows narrow peaks ranged from 2–50 nm, indicating the existence of mesopores in the CoP-NTs. The above results suggest that CoP-NTs could provide higher porosity and a larger specific surface area compared to CoP-NPs and W-CoP-NTs for faster mass diffusion and electron transfer during the electrocatalytic processes. To directly investigate the number of active sites (n), cyclic voltammograms (CVs) were collected between −0.4 V and +0.6 V *vs.* RHE (Fig. 4c). According to the previous report,[41] the integrated charge over the whole potential range should be proportional to the total number of active sites since it is difficult to assign the observed peaks to a given redox couple. Thus, by assuming a one-electron process for both the reduction and oxidation processes, the calculated number of active sites is 7.06×10^{-8} mol for CoP-NTs, which is nearly three times that (2.35×10^{-8} mol) for CoP-NPs. Therefore, the positively charged Co centers and negatively charged basic P centers in CoP-NTs could provide more hydride-acceptor and proton-acceptor centers, while the P centers will further promote the formation of cobalt hydride, thus largely facilitating the following H_2 evolution by electrochemical desorption as illustrated in Fig. 4d.

Since the catalytic efficiency of an electrocatalyst largely depends on its surface structure, a series of CoP-NTs (*i.e.*, CoP-NTs-2, CoP-NTs-5, CoP-NTs-8 and CoP-NTs-11) have been fabricated by varying the ratios between NaH_2PO_2 and Co_3O_4-NTs to study the influence of the phosphorization degree on their catalytic activities. As shown in Fig. 5a and b, by using a lower concentration ratio (≤8) of NaH_2PO_2, CoP-NTs-2 and CoP NTs-5 still keep well-reserved tubular structures. However, when the precursor concentration ratio increases to 11, the phosphorization reaction of Co_3O_4-NTs is more completed to form thicker tube walls for CoP-NTs-11 (Fig. 5c), which may deteriorate the mass and electron transfer within the CoP nanotubes. The phosphorization degree of Co_3O_4-NTs is further indicated by the XRD patterns. As displayed in Fig. S6,† the intensities of the characteristic diffraction peaks corresponding to the (011), (111) and (211) crystal planes of CoP-NTs increase with the increased concentration ratio between NaH_2PO_2 and Co_3O_4-NTs, demonstrating a gradually completed phosphorization process. Under a low phosphorization degree, the LSV curve of CoP-NTs-2 exhibits very weak catalytic performance to drive a current density of 10 mA cm^{-2} during the HER process (Fig. 6a). Satisfyingly, increased electrocatalytic performances with decreased overpotentials are observed for CoP-NTs-5 (224 mV) and CoP-NTs-8 (152 mV), respectively, implying that the HER activity is improved with increasing phosphorus content for the gradually increased active metal-phosphorus bondings on the surface of the electrocatalyst (Table 1). Nonetheless, the CoP-NTs-11 electrode displays inferior performance at the overpotential of 169 mV, which may be ascribed to the limited electrolyte and charge transfer over the thick and solid nanotube walls. Therefore, the proper phosphorization transition of Co_3O_4-NTs into CoP-NTs plays a crucial role in construction of tubular CoP-NTs as efficient "hydrogen deliverers" toward the HER for fast ion migration and electron transfer. As expected, all of the corresponding Tafel plots indicate a Volmer–Heyrovsky mechanism, which consists of a rapid discharge Volmer reaction and a rate-limiting electrochemical desorption Heyrovsky reaction process.

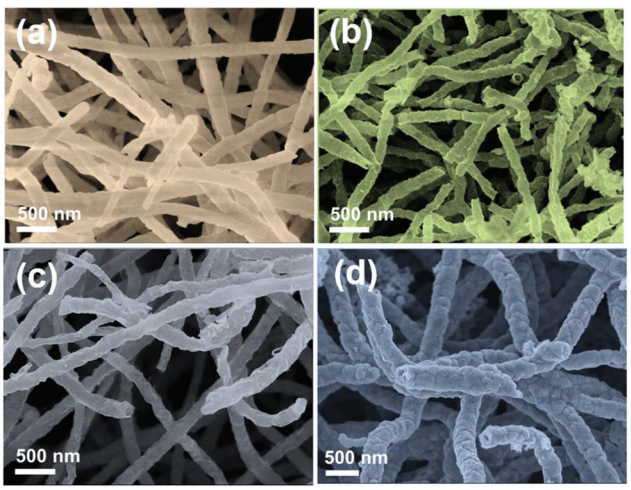

Fig. 5 FESEM images of CoP-NTs-2 (a), CoP-NTs-5 (b), CoP-NTs-8 (c) and CoP-NTs-11 (d).

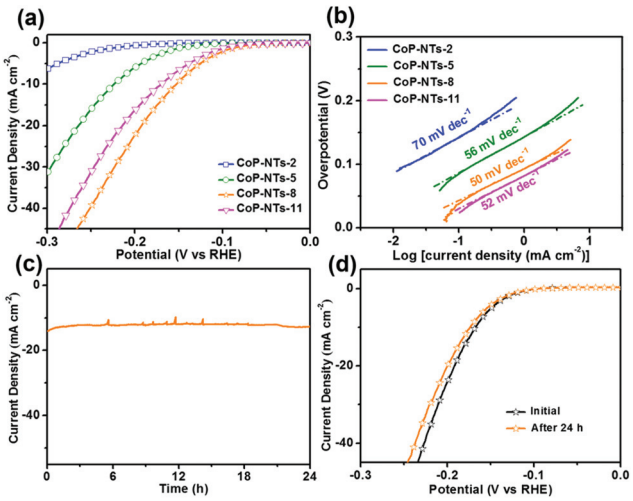

Fig. 6 (a) LSV polarization curves at a scan rate of 2 mV s^{-1}. (b) The corresponding Tafel plots of CoP-NTs-2, CoP-NTs-5, CoP-NTs-8 and CoP-NTs-11, respectively. (c) The time-dependent current density curve for the CoP-NTs-8 electrode operated under a static overpotential of 170 mV for 24 h. (d) LSV polarization curves before and after the durability test for the CoP-NTs-8 electrode.

Table 1 Comparisons of the HER catalytic parameters of different CoP-based materials

Catalyst	Onset overpotential (η, mV *vs.* RHE)	Tafel slope (b, mV dec^{-1})	η at 10 mA cm^{-2} (mV *vs.* RHE)
CoP-NPs	73	57	211
W-CoP-NTs	59	52	230
CoP-NTs-2	94	70	—
CoP-NTs-5	87	56	224
CoP-NTs-8	53	50	152
CoP-NTs-11	45	52	169
Pt/C	0	31	—

The durability is another critical criterion to evaluate the performance of a HER electrocatalyst. As shown in Fig. 6c, the time-dependent current density curve of CoP-NTs-8 was recorded under a static overpotential of 170 mV at a mass loading of 0.35 mg cm^{-2}. Notably, no appreciable decay of the cathodic current density is observed after 24 h scanning, manifesting an outstanding cycling stability of the as-prepared CoP-NTs-8 electrode in acidic media. Meanwhile, the polarization curves of the CoP-NTs-8 electrode before and after the durability test were recorded at a scan rate of 2 mV s^{-1} as displayed in Fig. 6d, which manifests only a slight increase of 7 mV for the overpotential over 24 h of continuous operation. The negligible deterioration might be caused by the production of H_2 bubbles, which gather around the electrode and suppress further reactions. The outstanding durability of the CoP-NT electrode makes it promising as a highly stable HER electrocatalyst for long-time cycling operations.

Conclusions and outlook

In summary, we have reported a facile strategy to fabricate mesoporous CoP-NTs with a three-dimensional network structure through the combination of electrospinning, pre-oxidation, pyrolysis and phosphorization treatments. Under optimized pre-oxidation and phosphorization conditions, the CoP-NTs exhibit a unique 1D hollow tubular structure instead of forming severe aggregations, which provide a long range order and large specific surface area for rapid ion diffusion, fast electron transfer, and the efficient electrochemical interactions between the electrolyte and electrocatalyst. Therefore, the CoP-NT electrode demonstrates an excellent electrocatalytic activity toward the HER with a low onset overpotential of 53 mV, a low overpotential of 152 mV to drive a high current density of 10 mA cm^{-2}, and a small Tafel slope of 50 mV dec^{-1}, being promising as an inexpensive and high-efficiency electrocatalyst for hydrogen production.

Conflicts of interest

There are no conflicts to declare.

Acknowledgements

The authors are grateful for the financial support from the National Natural Science Foundation of China (51373037, 51433001, and 21604010), the China Postdoctoral Science Foundation (2016M600268), the Program of Shanghai Academic Research Leader (17XD1400100), and the "Chenguang Program" supported by Shanghai Education Development Foundation and Shanghai Municipal Education Commission.

References

1 C. G. Morales Guio, L. A. Stern and X. Hu, *Chem. Soc. Rev.*, 2014, **43**, 6555–6569.
2 Y. Jiao, Y. Zheng, M. Jaroniec and S. Z. Qiao, *Chem. Soc. Rev.*, 2015, **44**, 2060–2086.
3 X. X. Zou and Y. Zhang, *Chem. Soc. Rev.*, 2015, **44**, 5148–5180.
4 Y. Yan, B. Y. Xia, Z. C. Xu and X. Wang, *ACS Catal.*, 2014, **4**, 1693–1705.
5 S. Bai, C. M. Wang, M. S. Deng, M. Gong, Y. Bai, J. Jiang and Y. J. Xiong, *Angew. Chem., Int. Ed.*, 2014, **53**, 12120–12124.
6 H. J. Yin, S. L. Zhao, K. Zhao, A. Muqsit, H. J. Tang, L. Chang, H. J. Zhao, Y. Gao and Z. Y. Tang, *Nat. Commun.*, 2015, **6**, 6430.
7 Z. X. Fan, Z. M. Luo, X. Huang, B. Li, Y. Chen, J. Wang, Y. L. Hu and H. Zhang, *J. Am. Chem. Soc.*, 2016, **138**, 1414–1419.
8 J. Wang, H. Zhang and X. Wang, *Small Methods*, 2017, **1**, 1700118.
9 M. A. Lukowski, A. S. Daniel, F. Meng, A. Forticaux, L. Li and S. Jin, *J. Am. Chem. Soc.*, 2013, **135**, 10274–10277.
10 W. F. Chen, S. Iyer, K. Sasaki, C. H. Wang, Y. Zhu, J. T. Muckerman and E. Fujita, *Energy Environ. Sci.*, 2013, **6**, 1818–1826.
11 J. Kibsgaard, Z. Chen, B. N. Reinecke and T. F. Jaramillo, *Nat. Mater.*, 2012, **11**, 963–969.
12 J. F. Callejas, C. G. Read, C. W. Roske, N. S. Lewis and R. E. Schaak, *Chem. Mater.*, 2016, **28**, 6017–6044.
13 Q. P. Lu, Y. F. Yu, Q. L. Ma, B. Chen and H. Zhang, *Adv. Mater.*, 2016, **28**, 1917–1933.
14 Y. M. Shi and B. Zhang, *Chem. Soc. Rev.*, 2016, **45**, 1529–1541.
15 J. H. Wang, W. Cui, Q. Liu, Z. C. Xing, A. M. Asiri and X. P. Sun, *Adv. Mater.*, 2016, **28**, 215–230.
16 Y. Yan, B. Y. Xia, B. Zhao and X. Wang, *J. Mater. Chem. A*, 2016, **4**, 17587–17603.
17 P. Jiang, Q. Liu, C. J. Ge, W. Cui, Z. H. Pu, A. M. Asiri and X. P. Sun, *J. Mater. Chem. A*, 2014, **2**, 14634–14640.
18 J. Q. Tian, Q. Liu, A. M. Asiri and X. P. Sun, *J. Am. Chem. Soc.*, 2014, **136**, 7587–7590.
19 Y. Pan, Y. Lin, Y. J. Chen, Y. Q. Liu and C. G. Liu, *J. Mater. Chem. A*, 2016, **4**, 4745–4754.

20 Y. P. Zhu, Y. P. Liu, T. Z. Ren and Z. Y. Yuan, *Adv. Funct. Mater.*, 2015, **25**, 7337–7347.
21 Y. Feng, X. Y. Yu and U. Paik, *Chem. Commun.*, 2016, **52**, 1633–1636.
22 E. J. Popczun, C. G. Read, C. W. Roske, N. S. Lewis and R. E. Schaak, *Angew. Chem., Int. Ed.*, 2014, **53**, 5427–5430.
23 P. He, X. Y. Yu and X. W. Lou, *Angew. Chem., Int. Ed.*, 2017, **56**, 3897–3900.
24 J. L. Liu, Y. Yang, B. Ni, H. Y. Li and X. Wang, *Small*, 2017, **13**, 1602637.
25 J. F. Callejas, C. G. Read, E. J. Popczun, J. M. McEnaney and R. E. Schaak, *Chem. Mater.*, 2015, **27**, 3769–3774.
26 X. Y. Ye, X. J. Huang and Z. K. Xu, *Chin. J. Polym. Sci.*, 2012, **30**, 130–137.
27 Y. E. Miao, F. Li, H. Y. Lu, J. J. Yan, Y. P. Huang and T. X. Liu, *Compos. Commun.*, 2016, **1**, 15–19.
28 X. Lu, C. Wang, F. Favier and N. Pinna, *Adv. Energy Mater.*, 2017, **7**, 1601301.
29 S. Peng, L. Li, J. Kong Yoong Lee, L. Tian, M. Srinivasan, S. Adams and S. Ramakrishna, *Nano Energy*, 2016, **22**, 361–395.
30 J. W. Jung, C. L. Lee, S. Yu and I. D. Kim, *J. Mater. Chem. A*, 2016, **4**, 703–750.
31 Q. X. Guan, C. P. Sun, R. G. Li and W. Li, *Catal. Commun.*, 2011, **14**, 114–117.
32 L. L. Li, C. Chen, L. Chen, Z. X. Zhu and J. L. Hu, *Environ. Sci. Technol.*, 2014, **48**, 3372–3377.
33 Q. Liu, J. Q. Tian, W. Cui, P. Jiang, N. Y. Cheng, A. M. Asiri and X. P. Sun, *Angew. Chem., Int. Ed.*, 2014, **53**, 6710–6714.
34 E. J. Popczun, C. W. Roske, C. G. Read, J. C. Crompton, J. M. McEnaney, J. F. Callejas, N. S. Lewis and R. E. Schaak, *J. Mater. Chem. A*, 2015, **3**, 5420–5425.
35 M. Li, X. T. Liu, Y. P. Xiong, X. J. Bo, Y. F. Zhang, C. Han and L. P. Guo, *J. Mater. Chem. A*, 2015, **3**, 4255–4265.
36 C. D. Wang, J. Jiang, X. L. Zhou, W. L. Wang, J. Zuo and Q. Yang, *J. Power Sources*, 2015, **286**, 464–469.
37 Z. C. Xing, Q. Liu, A. M. Asiri and X. P. Sun, *ACS Catal.*, 2015, **5**, 145–149.
38 Y. Xu, R. Wu, J. F. Zhang, Y. M. Shi and B. Zhang, *Chem. Commun.*, 2013, **49**, 6656–6658.
39 H. Zhu, J. F. Zhang, R. P. Yanzhang, M. L. Du, Q. F. Wang, G. H. Gao, J. D. Wu, G. M. Wu, M. Zhang, B. Liu, J. M. Yao and X. W. Zhang, *Adv. Mater.*, 2015, **27**, 4752–4759.
40 Y. P. Tian, Z. H. Zhang and Y. Q. Miao, *J. Electrochem. Soc.*, 2016, **163**, H625–H629.
41 P. Jiang, Q. Liu and X. P. Sun, *Nanoscale*, 2014, **6**, 13440–13445.

